# Numerical stabilization methods for level-set-based ice front migration

Gong Cheng[1], Mathieu Morlighem[1], and G. Hilmar Gudmundsson[2]

[1]Department of Earth Sciences, Dartmouth College, Hanover, NH 03755, USA
[2]Department of Geography and Environmental Sciences, Northumbria University, Newcastle upon Tyne, UK

**Correspondence:** Gong Cheng (gong.cheng@dartmouth.edu)

**Abstract.** Numerical modeling of ice sheet dynamics is a critical tool for projecting future sea-level rise. Among all the processes responsible for the loss of mass of the ice sheets, enhanced ice discharge triggered by the retreat of marine terminating glaciers is one of the key drivers. Numerical models of ice sheet flow are therefore required to include ice front migration in order to reproduce today's mass loss and be able to predict their future. However, the discontinuous nature of calving poses
5 a significant numerical challenge for accurately capturing the motion of the ice front. In this study, we explore different stabilization techniques combined with varying reinitialization strategies to enhance the numerical stability and accuracy of solving the level-set function, which tracks the position of the ice front. Through rigorous testing on an idealized domain with a semicircular and a straight-line ice front, including scenarios with diverse front velocities, we assess the performance of these techniques. The findings contribute to advancing our ability to model ice sheet dynamics, specifically calving processes, and
10 provide valuable insights into the most effective strategies for simulating and tracking the motion of the ice front.

## 1 Introduction

Ice sheet numerical modeling is the best tool to make future sea-level rise projections (e.g., Seroussi et al., 2020; Goelzer et al., 2020; IPCC, 2021). One key process that significantly contributes to mass loss is the retreat of marine terminating glaciers
15 (Mouginot et al., 2019; Choi et al., 2021; Pattyn and Morlighem, 2020). For example, in Greenland, the increased ice discharge is mainly driven by the retreat of glacier fronts (King et al., 2020), which is a direct consequence of calving and undercutting at the ice front (Wood et al., 2021; Mouginot et al., 2019), possibly intensified by increased runoff and ocean temperatures (Black and Joughin, 2023). As Greenland has very few ice shelves, ice front retreat predominantly comprises small yet frequent calving events (Black and Joughin, 2023; Cheng et al., 2021). Future projections emphasize that ice front retreat will continue
20 to be a primary driver of Greenland's mass loss by 2100 (Choi et al., 2021). Incorporating moving boundaries into numerical ice sheet models is a vital step in advancing our understanding of ice loss mechanisms and improving the accuracy of future sea-level rise projections (Crawford et al., 2021; Bondzio et al., 2017; Cheng et al., 2022).

Ice sheets are commonly modeled as incompressible fluids governed by conservation laws (e.g., Greve and Blatter, 2009), with empirical calving laws to predict calving rates at the ice front (Pollard et al., 2015; Morlighem et al., 2016). These calving
25 laws are parameterizations developed based on physical principles and observations, which offer computationally efficient and relatively straightforward expressions for calving rates (Benn and Astrom, 2018; Choi et al., 2018). In these parameterizations, the boundary of the model, which is generally the ice front, needs to be adjusted dynamically during the transient simulation. The way ice front migration is typically handled is through a level-set function, which is a signed distance function defined over the entire computational domain with the zero level-set contour representing the ice front position (e.g., Bondzio et al.,
30 2016; Morlighem et al., 2016). The motion of the level-set function is determined by solving an advection equation, where the difference between the ice velocity and the calving (and melting) rate at the zero-contour governs the evolution (Morlighem et al., 2016).

However, solving numerically the level-set function is challenging, especially when using the finite element method (FEM), as it can lead to instabilities due to the unbounded gradient of the solution (Larson and Bengzon, 2013). To address this is-
35 sue, stabilization techniques are employed to enforce the boundedness of the solution. Commonly used stabilization methods include artificial diffusion (AD), streamline-upwinding (SU), and Streamline Upwind Petrov–Galerkin (SUPG) (MacAyeal, 1989; Eriksson, 1996; Brooks and Hughes, 1982). Additionally, the transient solution of the level-set function may not always maintain its signed distance property due to the inhomogeneity of the velocity field and the accumulation of numerical errors over time, particularly through the diffusion introduced by numerical stabilization methods. Therefore, geometrical reinitial-
40 ization is generally necessary during transient simulations to restore the signed distance function property.

In this paper, we aim to investigate and compare various stabilization techniques in combination with different choices of reinitialization intervals, implemented in the Ice-sheet and Sea-level System Model v4.23 (ISSM, Larour et al., 2012; ISSM Team, 2023) and Úa 2019b (Gudmundsson et al., 2019; Gudmundsson, 2020). We present different stabilization and reinitialization procedures, and apply them to solve the level-set equation on an idealized domain featuring a semicircular ice front
45 shape (and a straight-line ice front shape case in the appendix). To evaluate the effectiveness of the stabilization techniques and reinitialization strategies, we perform several tests on three different spatially varying rates of ice front migration, encompassing both low and high-speed scenarios. By exploring these approaches, we seek to investigate which combination leads to the best stability and accuracy of simulating the level-set function and effectively tracks the motion of the ice front in ice sheet models.

## 2 Method

The level-set function $\phi(\boldsymbol{x}, t)$ is a scalar field defined on a two-dimensional domain $\Omega$ with zero contours implicitly representing the ice front position at every given time $t$. Conventionally, the level-set function is set to be negative in the ice-covered region and positive in the ice-free region (Morlighem et al., 2016), in order for the gradient of the level-set to be normal outward pointing to the ice front. The absolute value of the level-set is the closest distance from $\boldsymbol{x}$ to the ice front contour $\phi = 0$. Given

55  an initial condition $\phi(\boldsymbol{x}, 0) = \phi_0$, the evolution of the level-set function $\phi(\boldsymbol{x}, t)$ is governed by the advection equation

$$\frac{\partial \phi}{\partial t} + \boldsymbol{v}_f \cdot \nabla \phi = 0, \quad \boldsymbol{x} \in \Omega, \, t \in [0, T] \tag{1}$$

where $\boldsymbol{v}_f$ is the front velocity of the level-set, which is the difference between the ice velocity, $\boldsymbol{v}$, and the calving rate of $c$, which is generally oriented perpendicular to the ice front:

$$\boldsymbol{v}_f = \boldsymbol{v} - c \, \mathbf{n}, \tag{2}$$

60  where $\mathbf{n}$ is the outward unit normal vector of the level-set (Bondzio et al., 2016; Morlighem et al., 2016).

In order to solve (1) with the FEM, we introduce a Hilbert space $\mathcal{H}^1(\Omega)$ and define the variational form as: find $\phi \in \mathcal{H}^1(\Omega)$ such that for all the test function $\psi \in \mathcal{H}^1(\Omega)$ the equation

$$\int_\Omega \left( \frac{\partial \phi}{\partial t} \psi + (\boldsymbol{v}_f \cdot \nabla \phi) \psi \right) \, \mathrm{d}\Omega = 0, \tag{3}$$

is satisfied. After replacing the space $\mathcal{H}^1(\Omega)$ by a continuous piecewise linear space $\Phi_h$, the solution of (3) is then the numer-
65  ical solution of (1). However, it is well known that (3) gives spurious oscillatory solutions without stabilization (Larson and Bengzon, 2013; dos Santos et al., 2021).

## 2.1 Stabilization

The potential methods to stabilize (3) are, for example, artificial diffusion, streamline upwinding, streamline upwinding Petrov-Galerkin, etc. Among them, the simplest way to stabilize an advection equation is to add an additional diffusion term in the
70  variational form (3) such that

$$\int_\Omega \left( \frac{\partial \phi}{\partial t} \psi + (\boldsymbol{v}_f \cdot \nabla \phi) \psi + \nabla \phi \cdot \boldsymbol{\kappa} \nabla \psi \right) \, \mathrm{d}\Omega = 0, \tag{4}$$

where, in two dimensions, the coefficient of the artificial diffusion term is a scalar

$$\kappa = \frac{1}{2} \sqrt{h_x^2 v_x^2 + h_y^2 v_y^2}, \tag{5}$$

where $h_x$ and $h_y$ are the characteristic mesh sizes in $x$ and $y$ directions, $v_x$ and $v_y$ are the $x$ and $y$ components of the front
75  velocity $\boldsymbol{v}_f$.

The streamline upwinding stabilization follows the same variational form as the artificial diffusion in (4), but the coefficient is modified from (5), to only add diffusion along the direction of the velocity, $\boldsymbol{v}_f$, by using

$$\boldsymbol{\kappa} = \frac{h}{2\|\boldsymbol{v}_f\|} \boldsymbol{v}_f \otimes \boldsymbol{v}_f, \tag{6}$$

where $h = \sqrt{h_x^2 + h_y^2}$ and $\otimes$ is the Kronecker product. Due to the large dissipation introduced by these two stabilization
80  methods, they are extremely stable but only have first-order accuracy (dos Santos et al., 2021).

A more accurate stabilization method is the Streamline upwind Petrov–Galerkin (SUPG, Brooks and Hughes, 1982), which modifies the test function to be $\hat{\psi} = \psi + \mu \boldsymbol{v}_f \cdot \nabla \psi$ in the variational form (3) such that

$$\int_\Omega \left( \frac{\partial \phi}{\partial t} + \boldsymbol{v}_f \cdot \nabla \phi \right) (\psi + \mu \boldsymbol{v}_f \cdot \nabla \psi) \ \mathrm{d}\Omega = 0, \tag{7}$$

where $\mu = \frac{h}{2 \| \boldsymbol{v}_f \|}$ is a mesh dependent coefficient (dos Santos et al., 2021).

85    In Úa, a forward-and-backward (FAB) diffusion term is added to the variational form (7) stabilized by SUPG. The FAB term is derived from the potential

$$\mathcal{P} = \frac{1}{pq} \int_\Omega \left( \| \nabla \phi \|^q - 1 \right)^p \, d\Omega \tag{8}$$

for which the directional derivative is

$$D_{\delta \phi} \mathcal{P} = \int_\Omega \left( \| \nabla \phi \|^q - 1 \right)^{p-1} \| \nabla \phi \|^{q-2} \nabla \phi \cdot \nabla \delta \phi \, d\Omega \tag{9}$$

90    This results in the addition of a non-linear diffusion term to the level-set equation, with a diffusion coefficient

$$\kappa = \mu \left( \| \nabla \phi \|^q - 1 \right)^{p-1} \| \nabla \phi \|^{q-2}, \tag{10}$$

which is bounded for $\| \nabla \phi \| \to 0$, provided $q \geq 2$. For $p$ an even number, the diffusion term defined by Eq. (10) can be both negative and positive and is an example of a *forward-and-backward* (FAB) diffusion. Note that the minimum of the potential $\mathcal{P}$ in Eq. (8) is found for $\| \nabla \phi \| = 1$, i.e. when $\phi$ is a distance function.

## 95    2.2    Reinitialization

The formulation of the advection equation (1) only describes the evolution of the zero level-set contour, however, it does not guarantee that the level-set function is always a signed distance function due to the inhomogeneity of the front velocity. Indeed, as $\boldsymbol{v}_f$ is generally higher at the ice front than the far field, the gradient of the level-set function close to the zero contours tends to decrease during the transient simulation.

100    In ice sheet modeling, we only care about the position of the zero level-set contour, which is the ice front position. Therefore, a common practice is to reset the level-set function by calculating the signed distance every $n_R$ time steps. This is often called 'reinitialization' (Bondzio et al., 2016; Morlighem et al., 2016), and the reinitialization interval $n_R$ is the number of time steps between two consecutive reinitializations. However, as we show later in the numerical experiments, numerical errors highly depend on the reinitialization interval. Here, we are going to investigate different reinitialization intervals combined with the

105    four stabilization methods described in Section 2.1.

## 2.3 Error Quantification

In order to quantify the difference between two ice front positions represented by the level-set functions $\phi_1$ and $\phi_2$, we introduce a misfit metric $d(\phi_1, \phi_2)$ such that

$$d(\phi_1, \phi_2) = \frac{\text{sgn}(\phi_1) - \text{sgn}(\phi_2)}{2}, \tag{11}$$

110   where

$$\text{sgn}(\phi) = \begin{cases} -1, & \phi < 0, \\ 0, & \phi = 0, \\ 1, & \phi > 0, \end{cases} \tag{12}$$

converts a level-set function to a sign function with $-1$ on the ice-covered side of the zero contour and $1$ on the ice-free side of the contour. Therefore, if $\phi_1$ is ahead of $\phi_2$ in terms of the ice front positions (more advance), the misfit area in $d(\phi_1, \phi_2)$ will be negative.

115   We integrate the absolute misfit over the whole domain, $\Omega$, and get a metric

$$\mathcal{J}(\phi_1, \phi_2) = \int\limits_{\Omega} |d(\phi_1, \phi_2)| \, \mathrm{d}\Omega = \frac{1}{2} \int\limits_{\Omega} |\text{sgn}(\phi_1) - \text{sgn}(\phi_2)| \, \mathrm{d}\Omega, \tag{13}$$

which is actually the absolute misfit area between the two level-set functions.

## 3   Numerical experiments

We investigate the influence of the four stabilization methods described in section 2.1 combined with different choices of
120   reinitialization interval (section 2.2). We consider here a semicircle-shaped initial ice front as shown in Figure 1. We apply analytical spatially and temporally varying velocity fields to mimic typical ice flow.

We run all the simulations on a two-dimensional square domain $\Omega(x, y) = [0, L] \times [0, L]$, with $L = 20$ km as the size of the domain. We create a structured triangular mesh on $\Omega$ with the element size of 100 m. In Figure 1, the calving front is represented by a semicircle (red) centered at $(c_x, c_y) = (\frac{5L}{8}, \frac{L}{2})$ with a radius of $r = \frac{L}{4}$, and the sidewalls of the fjord are in
125   blue and connect the semicircle to the right boundary of the domain. By construction, the width of the fjord is 10 km. The initial zero level-set is the red ice front together with the blue sidewalls, which has a closed form as $\{(x, y)|(x - c_x)^2 + (y - c_y)^2 = r^2, x \le c_x\} \bigcup \{(x, y)|x \in [c_x, L], y = c_y + r\} \bigcup \{(x, y)|x \in [c_x, L], y = c_y - r\}$.

We apply three distinct velocity fields to control the migration of the ice front. For simplicity, we assume that there is no ice flux across the side walls of the fjord so that the velocity field only contains a horizontal component as $\boldsymbol{v}_f = (v_x, 0)^T$. The
130   $x$-component of the velocity fields are given in Table 1.
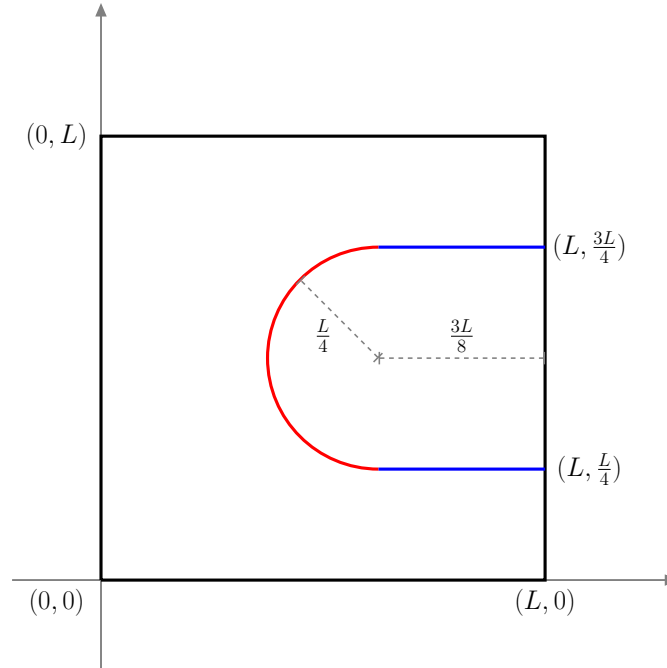
**Figure 1.** The domain of the semicircle-shaped ice front. The values close to the dashed grey lines are their lengths.

| Shape | Formula |
|---|---|
| Uniform | $v_x(x,y,t) = v(t)$ |
| Parabola | $v_x(x,y,t) = v(t)\left(1 - \left(\frac{y}{c_y} - 1\right)^2\right)$ |
| Triangle | $v_x(x,y,t) = v(t)\left(1 - \left|\frac{y}{c_y} - 1\right|\right)$ |

**Table 1.** The three shapes of front velocity at the ice front.

Temporal variations are introduced by flipping the sign of $v(t)$ (as in Table 1) every half year to mimic the typical annual cycle of the advance and retreat of an ice front such that

$$v(t) = \begin{cases} v_0, & t \in [nT, (n+\frac{1}{2})T), \\ -v_0, & t \in [(n+\frac{1}{2})T, (n+1)T), \end{cases} \tag{14}$$

where $T = 1$ year, $n = 0, 1, 2, 3, ..., N$ and $v_0$ is a velocity constant. We examine two scenarios with high ($v_0 = 5000$ m/a) and low ($v_0 = 1000$ m/a) velocity constants, respectively. All the simulations are run for $N = 50$ periods (or years), with a constant time step at $\Delta t = 0.005$ year to satisfy the CFL condition for both of the high and low-velocity scenarios. We reinitialize the

zero level-set contour with the interval $n_R = 1, 10, 100, 200$, which corresponds to a reinitialization every 2 days, two-thirds of a month, half a year, and one year. We also set a control run with no reinitialization ($n_R = \infty$) throughout the whole simulation period.

By applying the velocity for $\frac{T}{2}$ in one direction, then flipping the sign of $v_x$ for another $\frac{T}{2}$, the ice front is expected to return to its initial position $\phi_0$ after every period $T$. Furthermore, the analytical solution at any given time $t + nT$ should be identical to the solution at time $t$. Therefore, we use the numerical solution at $t \in [0, T)$ as the exact solution, and calculate the numerical error at $t + nT$ according to (13), with $\phi_1 = \phi(\boldsymbol{x}, t + nT)$ and $\phi_2 = \phi(\boldsymbol{x}, t)$.

## 4 Results

The misfit between the numerical and the exact solution under a uniform velocity field at the low-velocity setting ($v_0 = 1000$ m/a) after 1.5, 2 and 50 periods (or years) are shown in Figure 2 with $n_R = 1$, and in Figure 3 with $n_R = 100$ for the four stabilization methods considered in this paper. The misfit at every time point is calculated according to (11), where the area with negative values (blue in the figures) indicates the ice front from the numerical solution is downstream (i.e. further advanced) of the exact solution. The errors of all the cases in Figure 2 and 3 are almost evenly distributed along the ice front, and the total misfit grows as time increases. Figure 2 and 3 also indicate that using $n_R = 100$ gives more accurate results compared to reinitializing every time step ($n_R = 1$).

To facilitate a better comparison of the different stabilization, reinitialization, and velocity constant choices, we show the total absolute misfit in Figure 4, which is calculated according to (13) at the final time step $t = 50$ years for the uniform velocity field. The numerical errors tend to decrease as the reinitialization interval $n_R$ increases. Specifically, in Figure 4 (a), the four largest errors occur when the level-set function is reinitialized at every time step ($n_R = 1$), resulting in errors of 21.84 km$^2$ in AD, 16.92 km$^2$ in SU, 12.46 km$^2$ in SUPG, and 11.54 km$^2$ in SUPG+FAB. The spatial distributions of the errors are shown in Figure 2 (c), (f), (i), and (l). Given that the width of the fjord is 10 km, these errors correspond an average offset of the ice front of 1 to 2 km along the flow direction. After $n_R > 10$, the numerical errors remain almost constant, comparable to the ones of $n_R = \infty$, for all the stabilization methods employed. We find a similar pattern in the high-velocity ($v_0 = 5000$ m/a) cases in Figure 4 (b), where most of the numerical errors are approximately five times larger than those in the low-velocity ($v_0 = 1000$ m/a) cases in Figure 4 (a). However, there are exceptions in the high-velocity cases. For instance, reinitializing every time step does not introduce exceptionally large errors as we found in the low-velocity cases. Indeed, the largest numerical error (70.81 km$^2$) among all the experiments is achieved by the AD stabilization without reinitialization.

Although all four stabilization methods tend to overestimate the advance of the ice front, the choice of stabilization method has a significant impact on the misfit area, and SUPG+FAB exhibits the lowest numerical errors. In the low-velocity scenario, e.g. Figure 4 (a), with $n_R = 100$, the final misfit for SUPG+FAB is 0.38 km$^2$, whereas the errors for AD, SU, and SUPG are 8.33 km$^2$, 4.35 km$^2$, and 0.39 km$^2$, respectively. The spatial distributions of these errors are shown in Figure 3 (c), (f), (i), and (l), where the misfit achieved by SUPG is equivalent to an offset of the ice front by approximately 39 m, which is even less than half of the mesh size. Similarly, in the high-velocity scenario, the errors are scaled by the front velocity in all the choices
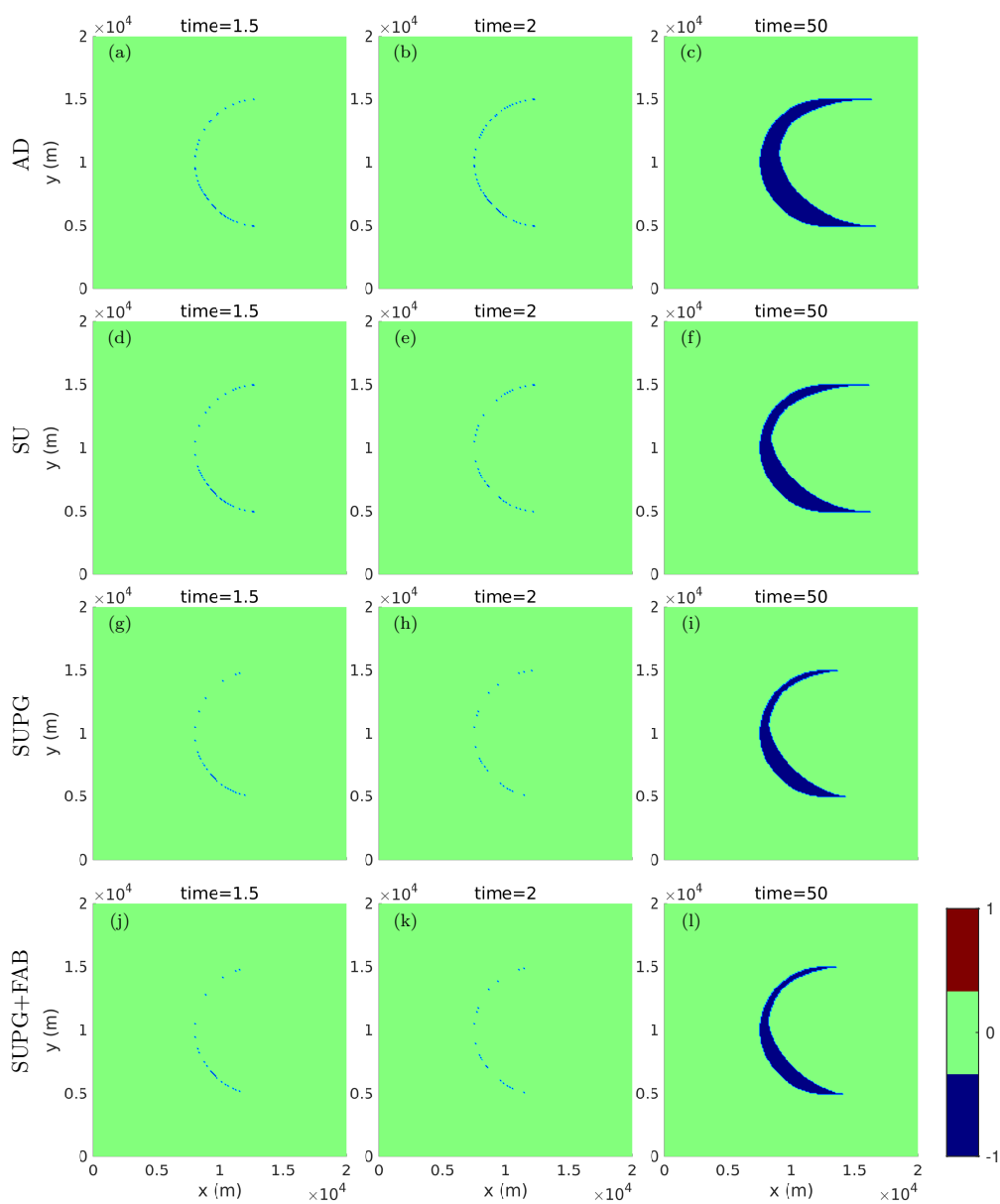
**Figure 2.** Misfit $d(\phi_1, \phi_2)$ of the solution at time $t$ (as $\phi_1$) and its exact solution (as $\phi_2$) at the reinitialization interval $n_R = 1$, and $v_0 = 1000$ m/a, with (a-c) AD, (d-f) SU, (g-i) SUPG, and (j-l) SUPG+FAB stabilizations.
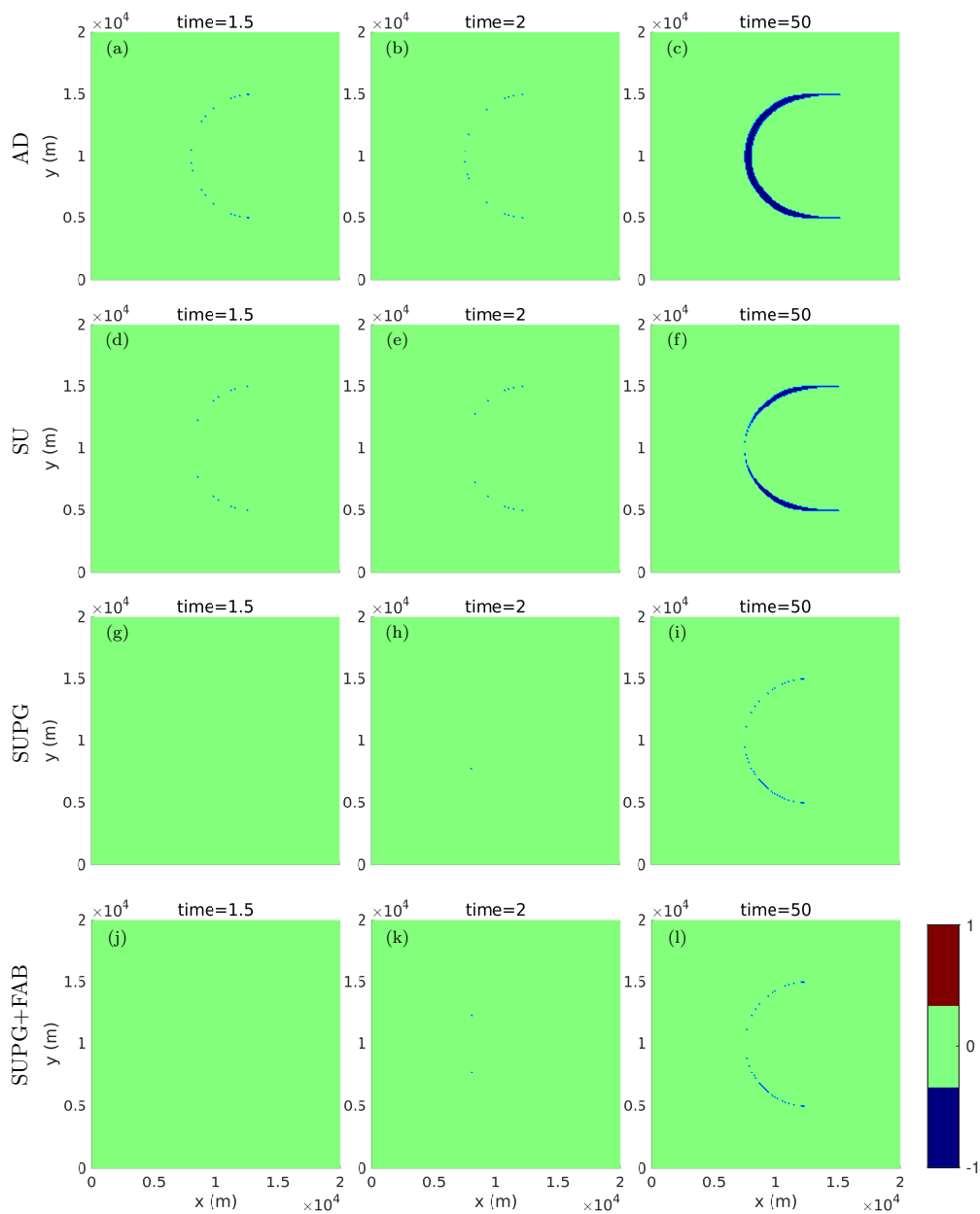
**Figure 3.** Misfit $d(\phi_1, \phi_2)$ of the solution at time $t$ (as $\phi_1$) and its exact solution (as $\phi_2$) at the reinitialization interval $n_R = 100$, and $v_0 = 1000$ m/a, with (a-c) AD, (d-f) SU, (g-i) SUPG, and (j-l) SUPG+FAB stabilizations.
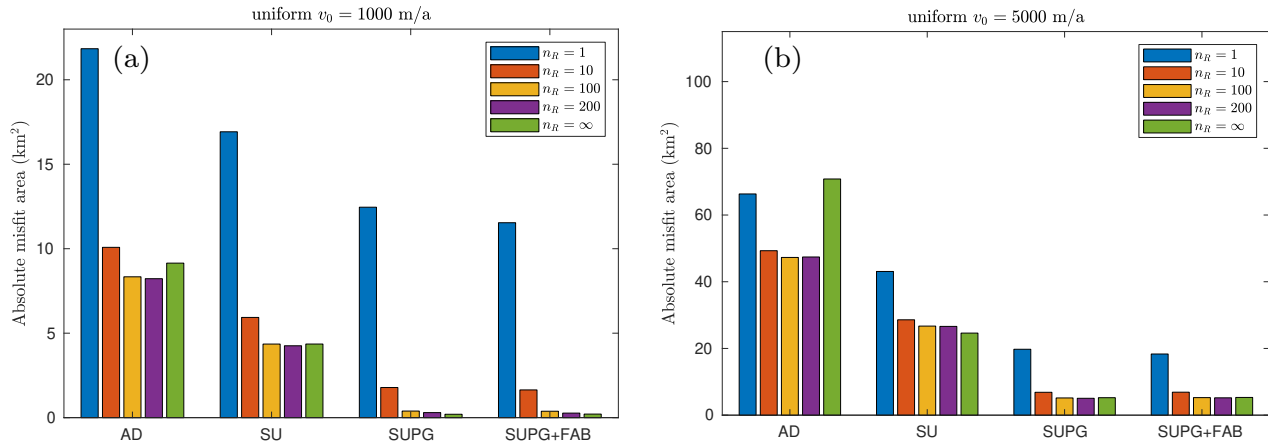
**Figure 4.** Total absolute misfit area at $T = 50$ for semicircle front with uniform velocity (a) $v_0 = 1000$ m/a and (b) $v_0 = 5000$ m/a. The $y$-axis in (b) is scaled by a factor of five for visualization purposes

of stabilizations with $n_R > 1$. For instance, in Figure 4 (b), with $n_R = 100$, the errors are $47.28$ km$^2$ in AD, $26.70$ km$^2$ in SU, $5.16$ km$^2$ in SUPG, and $5.26$ km$^2$ in SUPG+FAB.

We present the numerical errors at the final time step for the parabolic and triangular shape of velocity in Figure 5 for both low and high-velocity constants. Apparently, the shape of the velocity profile has a limited impact on the numerical errors. Nevertheless, the triangular velocity cases yield the smallest errors, while the parabolic velocity cases yield larger errors, but still smaller than the uniform velocity field scenario depicted in Figure 4.

## 5 Discussion

### 5.1 Reinitialization interval

From a finite-element method point of view, the reinitialization procedure is an $\mathcal{L}^2$ projection of the zero level-set contour onto the mesh (Larson and Bengzon, 2013). It can be shown that the numerical errors of the projection are proportional to the mesh sizes, and they accumulate as the number of reinitializations increases (i.e., as $n_R$ decreases). Furthermore, these errors are not only introduced during the projection but also transported and amplified by the governing equation (1) throughout the transient simulation. In the case of frequent reinitializations, such as $n_R = 1$, the dominant source of numerical error is the $\mathcal{L}^2$ projection, particularly evident when the front velocity is low ($v_0 = 1000$ m/a), as depicted in Figure 4 and 5. However, in the high-velocity scenario, the projection error becomes less significant compared to the numerical errors resulting from discretization and stabilization techniques, which then become the primary sources of error.

As $n_R$ increases, the numerical error decreases until no reinitialization is performed ($n_R = \infty$). However, in the absence of reinitialization, additional errors emerge due to the distortion of the gradient of the level-set function. The worst-case scenario observed in this study is the high uniform velocity case with AD at $n_R = \infty$ in Figure 4 (b), where the zero-contour of the final
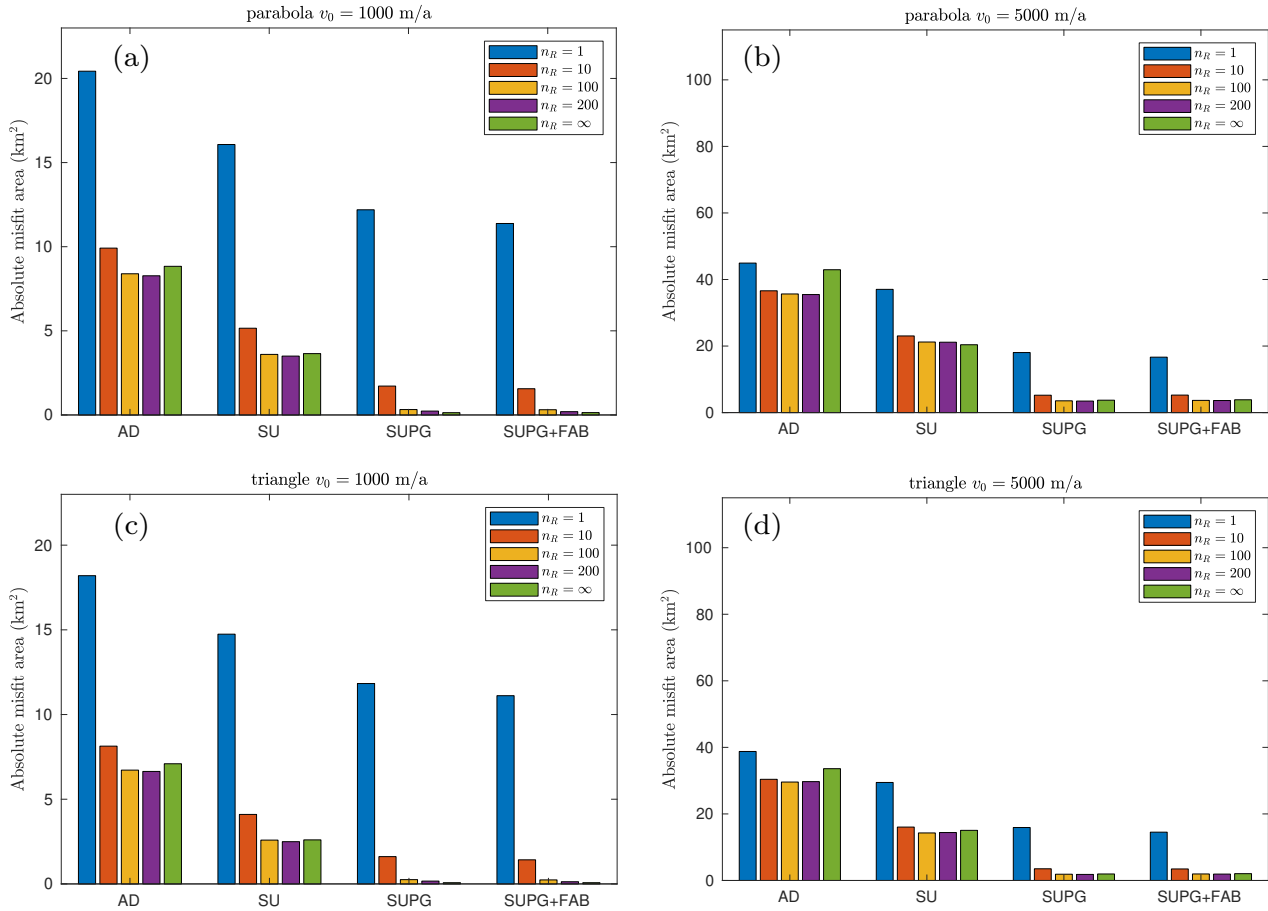
**Figure 5.** The total absolute misfit area at $T = 50$ with (a, b) parabola and (c, d) triangle shape velocity profiles. The left column has the velocity constant $v_0 = 1000$ m/a, and the right column is at $v_0 = 5000$ m/a.

level-set solution is nearly halfway into the fjord, resulting in a total misfit of $70.81$ km$^2$. This instance emphasizes the necessity

190    to reinitialize the level-set when solving level-set functions in transient simulations. It is worth noting that the numerical errors are not significantly affected by the interval of reinitialization as long as $n_R$ is sufficiently larger than 1. Consequently, for the remainder of this paper, the focus will be on discussing the cases with $n_R = 10, 100$, and $200$, while disregarding those with $n_R = 1$ and $n_R = \infty$

## 5.2   Stabilization method

195    The numerical errors in AD and SU are 5 to 20 times greater than those using SUPG and FAB as long as $n_R$ exceeds 1. The main source of the numerical errors in AD and SU is the diffusion term $\nabla \phi \cdot \boldsymbol{\kappa} \nabla \psi$ added in the advection equation (4), which

smears out the oscillations in the numerical solution and disperses the solution. The coefficient $\kappa$ controls the magnitude and direction of the additional diffusion.

In the AD case, the coefficient $\kappa$ is a scalar, which applies the diffusion to all directions with the same magnitude. In contrast, $\kappa$ contains an outer product of the front velocity in SU, which only adds diffusion along the flow direction of $v_f$. Therefore, the errors in SU are less dispersive than those in AD. Notably, the coefficients $\kappa$ in AD and SU are also controlled by the mesh size, such that the additional diffusion term vanishes as the mesh size becomes zero. In numerical ice sheet modeling, the mesh size is generally limited by data accuracy and computational capacity. Therefore, the weak solution of the stabilized equation (4) does not necessarily satisfy the variational formulation (3), and the corresponding errors are proportional to the mesh size (Larson and Bengzon, 2013).

On the other hand, the SUPG stabilizes the advection equation by adding an additional term in the test function as in (7), whose solution satisfies the weak form (3) almost everywhere, except for the position where the test functions equal to 0. In this sense, the numerical error is smaller than the other two stabilization methods. We therefore recommend using SUPG for the stabilization technique, together with a reinitialization interval greater than 10.

## 5.3 Front velocity

We anticipate the numerical errors to be scaled by the velocity magnitude when solving the advection equation using the finite element method (Biswas et al., 1994). As we construct the velocities in Table 1, for instance, with $v_0 = 1000$ m/a, the mean frontal velocity during the advance phase $t \in [nT, (n+\frac{1}{2})T]$ is 1000 m/a for the uniform shape, 916.7 m/a for the parabola and 750.0 m/a for the triangular shape. The corresponding numerical errors, at $n_R = 100$ with SUPG stabilization, are 0.39 km$^2$, 0.32 km$^2$, and 0.25 km$^2$, respectively. Furthermore, as we show in Figure 4 and 5, this relationship is found in almost all the reinitialization intervals $n_R > 1$, all stabilization techniques, both the low and high-velocity scenarios considered in this study.

## 5.4 Different front shapes

In Appendix A, we show the results of another shape of the ice front, which is a straight line with side walls orthogonal to the front. The final errors of the straight front cases with different stabilization methods, reinitialization intervals, and velocity shapes are more or less the same as those with the semicircle front. Although, the spatial distribution of the numerical error differs significantly between the two shapes. To further investigate the source of the numerical errors, we show the animations of the evolution of misfits in the supplementary material. In the straight front cases, the misfit is initiated at the two corners, where the ice front meets the side wall of the fjord, and then propagates to the center. In contrast, the semicircle case generates numerical errors that do not initiate from single sources, but grow along the entire ice front. The main reason for these differences is that the finite element method approximates the level-set function by projecting it onto a piecewise linear functional space. As a result, the sharp corners and the curved level-set contours are the places where most of the numerical errors occur. On average, these approximation errors are proportional to the mesh size, whereas the shape of the ice front actually has a negligible influence on the numerical errors.

# 6 Conclusions

230 We studied multiple stabilization methods implemented in ISSM and Úa for solving a level-set equation on an idealized geometry with with reinitialization interval that varies from once every time step up to no reinitialization. We found that SUPG and SUPG+FAB are considerably more accurate than the other two methods (AD and SU), for all choices of reinitialization interval, regardless of the front velocity and ice front shape. Using other stabilization methods results in more than ten times larger errors in ice front positions. An optimal choice of reinitialization interval is $n_R > 10$, which is equivalent to a time period

235 greater than 2.5 weeks in our experiments. Too frequent reinitialization can introduce additional numerical errors larger than any other sources. By identifying the most effective stabilization techniques and reinitialization intervals, we can improve the reliability and robustness of simulations, enabling more accurate predictions of ice sheet behavior and its influence on future sea-level rise.

*Code availability.* ISSM Version 4.23 is open source and available at https://doi.org/10.5281/zenodo.7850841 (ISSM Team, 2023). Úa

240 (v2019b) is open source and available at https://doi.org/10.5281/zenodo.3706624 (Gudmundsson, 2020). The code and data analyses used in this manuscript are available at https://doi.org/10.5281/zenodo.8376911.

*Video supplement.* The supplement video of the evolution of the misfit are available at https://doi.org/10.5281/zenodo.8400628
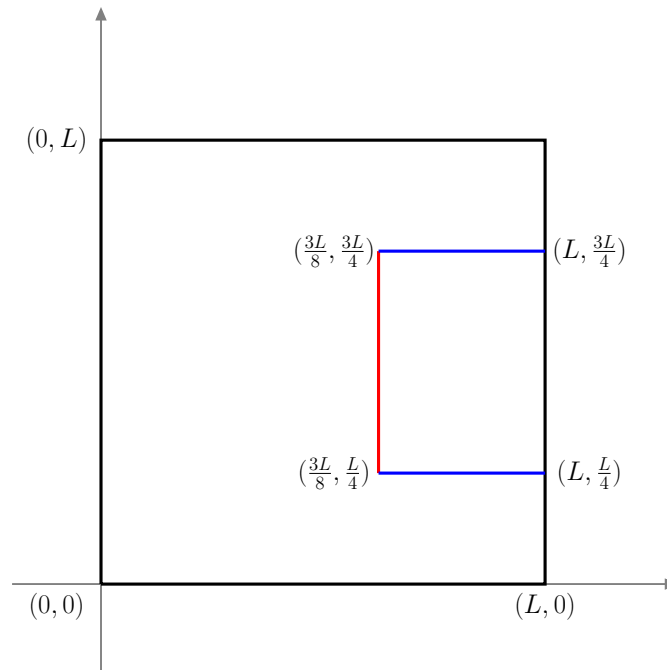
**Figure A1.** The domain of the straight ice front with the coordinates of the vertices.

## Appendix A: A straight ice front case

We present another ice front shape which is a straight line as shown in Figure A1. Similar as in Figure 1, the red line indicates

245  the ice front and the blue lines are the side walls of the fjord. With $L = 20$ km, the width of the fjord is also 10 km. We perform

the same experiments as described in Section 3, and show the total misfit at the final time step in Figure A2.
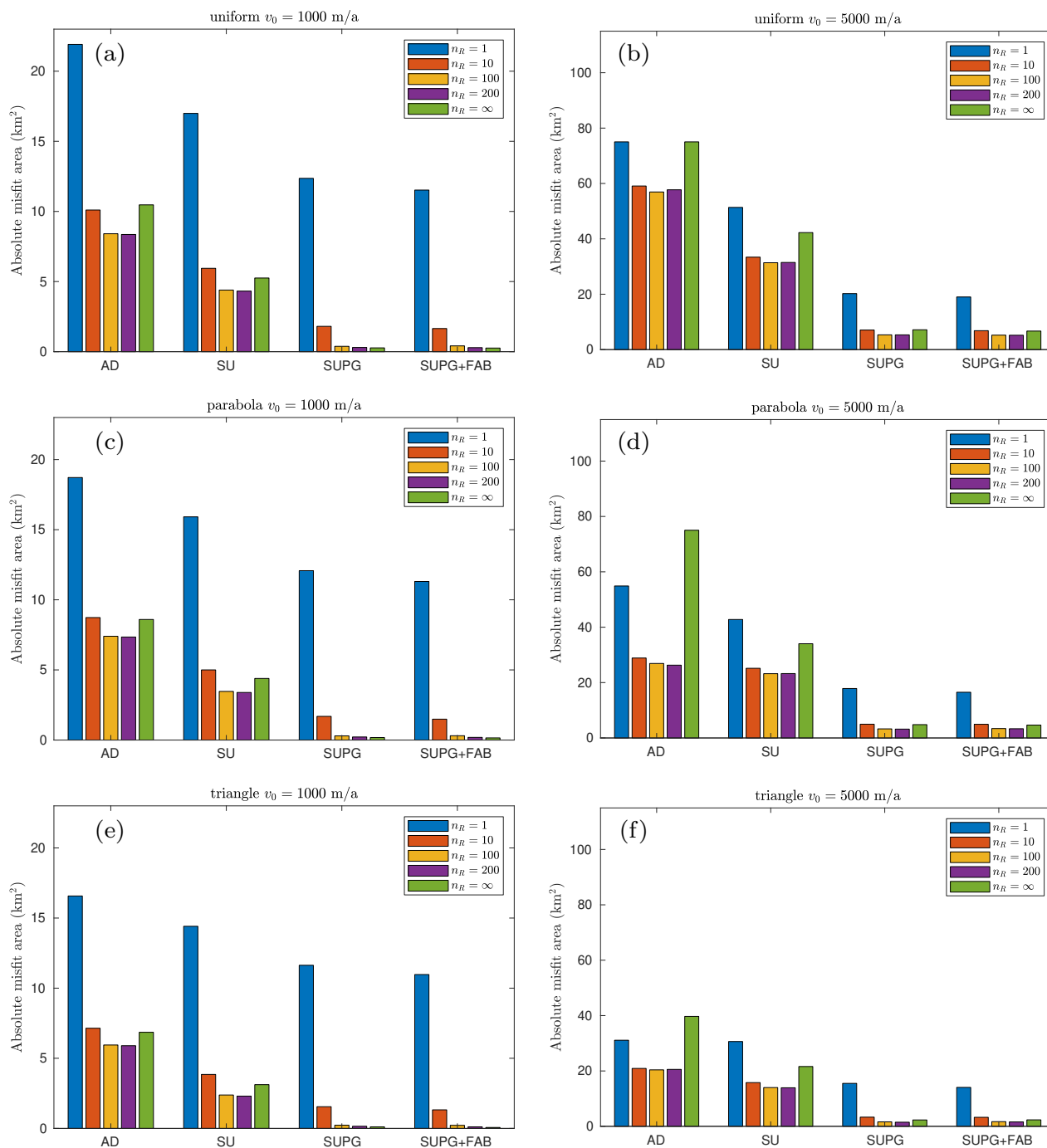
**Figure A2.** The total absolute misfit area at $T = 50$ with (a, b) uniform, (c,d) parabola, and (e, f) triangle shape velocity profiles for a straight ice front. The left column is in the low-velocity scenario with $v_0 = 1000$ m/a, and the right column is at $v_0 = 5000$ m/a.

*Author contributions.* GC, MM and HG designed the study. GC did the numerical computations. GC wrote the manuscript with input from MM and HG.

*Competing interests.* The authors declare that they have no conflict of interest.

250   *Acknowledgements.* This work was supported by the Heising Simons Foundation grant 2019-1161 and 2021-3059. This work is from the PROPHET project, a component of the International Thwaites Glacier Collaboration (ITGC). Support from National Science Foundation (NSF: Grant #1739031) and Natural Environment Research Council (NERC: Grants NE/S006745/1, NE/S006796/1 and NE/T001607/1). ITGC Contribution No. ITGC-XXX

# References

Benn, D. I. and Astrom, J. A.: Calving glaciers and ice shelves, Adv. Phys.: X, 3, https://doi.org/10.1080/23746149.2018.1513819, 2018.

Biswas, R., Devine, K. D., and Flahert, J. E.: Parallel, adaptive finite element methods for conservation laws, Appl. Numer. Math., 14, 255–283, https://doi.org/10.1016/0168-9274(94)90029-9, 1994.

Black, T. E. and Joughin, I.: Weekly to monthly terminus variability of Greenland's marine-terminatingoutlet glaciers, Cryosphere, 17, 1–13, https://doi.org/10.5194/tc-17-1-2023, 2023.

Bondzio, J., Morlighem, M., Seroussi, H., Kleiner, T., Ruckamp, M., Mouginot, J., Moon, T., Larour, E., and Humbert, A.: The mechanisms behind Jakobshavn Isbræ's acceleration and mass loss: A 3-D thermomechanical model study, Geophys. Res. Lett., 44, https://doi.org/10.1002/2017GL073309, 2017.

Bondzio, J. H., Seroussi, H., Morlighem, M., Kleiner, T., Rückamp, M., Humbert, A., and Larour, E.: Modelling calving front dynamics using a level-set method: application to Jakobshavn Isbræ, West Greenland, Cryosphere, 10, 497–510, https://doi.org/10.5194/tc-10-497-2016, 2016.

Brooks, A. N. and Hughes, T. J. R.: Streamline upwind Petrov-Galerkin formulations for convection dominated flows with particular emphasis on the incompressible Navier-Stokes equations, Comput. Methods Appl. Mech. Engrg., 32, 199–259, 1982.

Cheng, D., Hayes, W., Larour, E., Mohajerani, Y., Wood, M., Velicogna, I., and Rignot, E.: Calving Front Machine (CALFIN): glacial termini dataset and automated deep learning extraction method for Greenland, 1972–2019, The Cryosphere, 15, 1663–1675, https://doi.org/10.5194/tc-15-1663-2021, 2021.

Cheng, G., Morlighem, M., Mouginot, J., and Cheng, D.: Helheim Glacier's Terminus Position Controls Its Seasonal and Inter-Annual Ice Flow Variability, Geophys. Res. Lett., 49, e2021GL097 085, https://doi.org/10.1029/2021GL097085, 2022.

Choi, Y., Morlighem, M., Wood, M., and Bondzio, J. H.: Comparison of four calving laws to model Greenland outlet glaciers, Cryosphere, 12, 3735–3746, https://doi.org/10.5194/tc-12-3735-2018, 2018.

Choi, Y., Morlighem, M., Rignot, E., and Wood, M.: Ice dynamics will remain a primary driver of Greenland ice sheet mass loss over the next century, Nature Commun. Earth Environ., 2, 26, https://doi.org/10.1038/s43247-021-00092-z, 2021.

Crawford, A. J., Benn, D. I., Todd, J., Astrom, J. A., Bassis, J. N., and Zwinger, T.: Marine ice-cliff instability modeling shows mixed- mode ice-cliff failure and yields calving rate parameterization, Nat. Commun., 12, https://doi.org/10.1038/s41467-021-23070-7, 2021.

dos Santos, T. D., Morlighem, M., and Seroussi, H.: Assessment of numerical schemes for transient, finite-element ice flow models using ISSM v4.18, Geosci. Model Dev., 14, 2545–2573, https://doi.org/10.5194/gmd-14-2545-2021, 2021.

Eriksson, K.: Computational differential equations, Cambridge University Press, 1996.

Goelzer, H., Nowicki, S., Payne, A., Larour, E., Seroussi, H., Lipscomb, W. H., Gregory, J., Abe-Ouchi, A., Shepherd, A., Simon, E., Agosta, C., Alexander, P., Aschwanden, A., Barthel, A., Calov, R., Chambers, C., Choi, Y., Cuzzone, J., C., D., Edwards, T., Felikson, D., Fettweis, X., Golledge, N. R., Greve, R., Humbert, A., Huybrechts, P., Le clec'h, S., Lee, V., Leguy, G., Little, C., Lowry, D. P., Morlighem, M., Nias, I., Quiquet, A., Rückamp, M., Schlegel, N.-J.and Slater, D. A., Smith, R. S., Straneo, F., Tarasov, L., van de Wal, R., and van den Broeke, M.: The future sea-level contribution of the Greenland ice sheet: a multi-model ensemble study of ISMIP6, The Cryosphere, https://doi.org/10.5194/tc-14-3071-2020, 2020.

Greve, R. and Blatter, H.: Dynamics of Ice Sheets and Glaciers, Advances in Geophysical and Environmental Mechanics and Mathematics, Springer Science & Business Media, https://doi.org/10.1007/978-3-642-03415-2, 2009.

290    Gudmundsson, G. H., Paolo, F. S., Adusumilli, S., and Fricker, H. A.: Instantaneous Antarctic ice sheet mass loss driven by thinning ice shelves, Geophys. Res. Lett., 46, 13 903–13 909, https://doi.org/10.1029/2019GL085027, 2019.

Gudmundsson, H.: GHilmarG/UaSource: Ua2019b, https://doi.org/10.5281/zenodo.3706624, 2020.

IPCC: Climate Change 2021: The Physical Science Basis. Contribution of Working Group I to the Sixth Assessment Report of the Intergovernmental Panel on Climate Change, vol. In Press, Cambridge University Press, Cambridge, United Kingdom and New York, NY, USA,
295    https://doi.org/10.1017/9781009157896, 2021.

ISSM Team: Ice-sheet and Sea-level System Model source code, v4.23 r27696, https://doi.org/10.5281/zenodo.7850841, 2023.

King, M. D., Howat, I. M., Candela, S. G., Noh, M. J., Jeong, S., Noel, B. P. Y., van den Broeke, M. R., Wouters, B., and Negrete, A.: Dynamic ice loss from the Greenland Ice Sheet driven by sustained glacier retreat, Commun. Earth Environ., 1, https://doi.org/10.1038/s43247-020-0001-2, 2020.

300    Larour, E., Seroussi, H., Morlighem, M., and Rignot, E.: Continental scale, high order, high spatial resolution, ice sheet modeling using the Ice Sheet System Model (ISSM), J. Geophys. Res., 117, 1–20, https://doi.org/10.1029/2011JF002140, 2012.

Larson, M. G. and Bengzon, F.: The Finite Element Method: Theory, Implementation, and Applications, Springer Publishing Company, Incorporated, 2013.

MacAyeal, D. R.: Large-scale ice flow over a viscous basal sediment: Theory and application to Ice Stream B, Antarctica, J. Geophys. Res.,
305    94, 4071–4087, 1989.

Morlighem, M., Bondzio, J., Seroussi, H., Rignot, E., Larour, E., Humbert, A., and Rebuffi, S.-A.: Modeling of Store Gletscher's calving dynamics, West Greenland, in response to ocean thermal forcing, Geophys. Res. Lett., 43, 2659–2666, https://doi.org/10.1002/2016GL067695, 2016.

Mouginot, J., Rignot, E., Bjørk, A. A., van den Broeke, M., Millan, R., Morlighem, M., Noël, B., Scheuchl, B., and Wood, M.: Forty-six
310    years of Greenland Ice Sheet mass balance from 1972 to 2018, Proc. Natl. Acad. Sci., https://doi.org/10.1073/pnas.1904242116, 2019.

Pattyn, F. and Morlighem, M.: The uncertain future of the Antarctic Ice Sheet, Science, 367, 1331–1335, https://doi.org/10.1126/science.aaz5487, 2020.

Pollard, D., DeConto, R. M., and Alley, R. B.: Potential Antarctic Ice Sheet retreat driven by hydrofracturing and ice cliff failure, Earth Planet Sci. Lett., 412, 112 – 121, https://doi.org/10.1016/j.epsl.2014.12.035, 2015.

315    Seroussi, H., Nowicki, S., Payne, A. J., Goelzer, H., Lipscomb, W. H., Abe-Ouchi, A., Agosta, C., Albrecht, T., Asay-Davis, X., Barthel, A., Calov, R., Cullather, R., Dumas, C., Galton-Fenzi, B. K., Gladstone, R., Golledge, N. R., Gregory, J. M., Greve, R., Hattermann, T., Hoffman, M. J., Humbert, A., Huybrechts, P., Jourdain, N. C., Kleiner, T., Larour, E., Leguy, G. R., Lowry, D. P., Little, C. M., Morlighem, M., Pattyn, F., Pelle, T., Price, S. F., Quiquet, A., Reese, R., Schlegel, N.-J., Shepherd, A., Simon, E., Smith, R. S., Straneo, F., Sun, S., Trusel, L. D., Van Breedam, J., van de Wal, R. S. W., Winkelmann, R., Zhao, C., Zhang, T., and Zwinger, T.: ISMIP6 Antarctica: a multi-
320    model ensemble of the Antarctic ice sheet evolution over the 21$^{st}$ century, The Cryosphere, 14, 3033–3070, https://doi.org/10.5194/tc-14-3033-2020, 2020.

Wood, M., Rignot, E., Fenty, I., An, L., Bjørk, A., van den Broeke, M., Cai, C., Kane, E., Menemenlis, D., Millan, R., Morlighem, M., Mouginot, J., Noël, B., Scheuchl, B., Velicogna, I., Willis, J. K., and Zhang, H.: Ocean forcing drives glacier retreat in Greenland, Sci. Adv., 7, https://doi.org/10.1126/sciadv.aba7282, 2021.